Dependency of halo concentration on mass, redshift and fossilness in Magneticum hydrodynamic simulations

Antonio Ragagnin[1,2,3], Klaus Dolag[3,4], Lauro Moscardini [5,6,7],
Andrea Biviano[8], Mauro D'Onofrio[9]

[1] *Leibniz-Rechenzentrum (LRZ), Boltzmannstrasse 1, D-85748 Garching, Germany*
[2] *Excellence Cluster Universe, Boltzmannstrasse 2, D-85748 Garching, Germany*
[3] *Universitäts-Sternwarte, Fakultät für Physik, Ludwig-Maximilians Universität München, Scheinerstrasse 1, D-81679 München, Germany*
[4] *Max-Planck-Institut für Astrophysik, Karl-Schwarzschild Strasse 1, D-85748 Garching bei München, Germany*
[5] *Dipartimento di Fisica e Astronomia, Alma Mater Studiorum - Università di Bologna, via Piero Gobetti 93/2, I-40129 Bologna, Italy*
[6] *INAF - Osservatorio di Astrofisica e Scienza dello Spazio di Bologna, via Piero Gobetti 93/3, I-40129 Bologna, Italy*
[7] *INFN, Sezione di Bologna, viale Berti Pichat 6/2, I-40127 Bologna, Italy*
[8] *INAF - Osservatorio Astronomico di Trieste, via G.B. Tiepolo 11, 34143 Trieste, Italy*
[9] *Dipartimento di Fisica e Astronomia G. Galilei, UniversitÃă di Padova, Vicolo Osservatorio 3, I-35122 Padova, Italy*

18 October 2018

ABSTRACT
We study the dependency of the concentration on mass and redshift using three large N-body cosmological hydrodynamic simulations carried out by the Magneticum project. We find a negative trend on the mass-concentration plane and a slightly negative redshift dependency, in agreement with observations and other numerical works. We constrain the slope of the mass-concentration relation with an unprecedented mass range for hydrodynamic simulations. We also investigate the origin of the large scatter of concentration by studying the relation with the fossil parameter, defined as the stellar mass ratio between the central galaxy and the most massive satellite. We study the correlation between concentration and fossilness by following the evolution of haloes that undergo major merging events and in objects without activity. We find that the internal region keeps accreating satellites and this causes both an increase of the fossil parameter and a slow but steady decrease of the scale radius, which increases the concentration. Finally, we study the dependency of the concentration on the virial ratio and the energy term from the surface pressure E_s. We find that the relation between concentration, fossilness and E_s is due to the relation between E_s and the presence of in-falling/out-falling material.

1 INTRODUCTION

Most density profiles of dark matter haloes from both simulations and observations can be described using a Navarro Frank and White (NFW) profile (Navarro et al. (1996, 1997), see Borgani & Kravtsov (2011) for a review). Such density profile is modelled as a function of the radial distance r as:

$$\rho\left(r\right) = \frac{\rho_0}{\frac{r}{r_s}\left(1 + \frac{r}{r_s}\right)^2},$$

where r_s is a scale radius separating the internal and the external regions, and ρ_0 is four times the density at $r = r_s$.

As haloes do not have well defined boundaries, the virial radius R_{vir} is assumed to be the radius at which the density of the halo is the one of a theoretical virialised homogeneous spherical overdensity in an expanding universe. The density threshold is represented as $\Delta_{vir}\rho_{crit}$. Here ρ_{crit} is the critical density $\rho_{crit} \equiv 3H^2/4\pi G$ and Δ_{vir} is a parameter that depends on cosmology. For instance, $\Delta_{vir} \approx 178$ in an Einstein de Sitter cosmology (see Naderi et al. (2015) for a review).

More generally, in the literature, people prefer to make use of radii definitions that are independent of cosmology and refer to R_Δ as the radius that includes an over-density of $\Delta \cdot \rho_{crit}$. In the following analysis, we use both $\Delta = 200$ and $\Delta = 500$ and the corresponding radii R_{200} and R_{500}.

The concentration c_Δ is defined as $c_\Delta \equiv R_\Delta/r_s$ and quantifies how wide is the internal region of the cluster, compared to its radius. Bullock et al. (2001) is a pioneering theoretical work devoted to the study of the concentration in a ΛCDM universe. Their toy model based on an isolated spherical over-density, whose scale factor a at the collapse time is a_c, predicts a concentration $c \propto a/a_c$, where the proportionality constant is universal for all haloes.

Various literature works make a fit of the concentration as a power law of the halo mass and redshift. They mainly found a very low dependency of concentration on redshift and a slow but steady decrease of the concentration with mass (see e.g. Dutton & Macciò 2014; Merten et al. 2015). In comparing various works one must first consider carefully how the concentration is computed. Some theoretical works

(Ludlow et al. 2012; Prada et al. 2012) derive the dark matter concentration from the peak in the velocity dispersion instead of constraining r_s from a NFW fit of the dark matter density profile. The concentration computed with this technique is systematically higher than the concentration computed with a NFW fit, with a relative error of $1 - 10\%$ (see Meneghetti & Rasia 2013, who show that the two values can differ significantly).

On top of this, Lin et al. (2006) found that introducing non-radiative gas physics in numerical simulations increases the concentration, while Duffy et al. (2010) showed how the additional inclusion of AGN feedback decreases the halo concentration. The concentration produced by runs with AGN feedback increases as the halo mass decreases, up to a difference of $\approx 15\%$ for haloes with a mass of $M \approx 10^{11} M_\odot$. Simulations with various dark energy models, as in Dolag et al. (2004); De Boni (2013); De Boni et al. (2013), showed that in the $c - M$ relation the normalisation is sensitive to the cosmological parameters and Duffy et al. (2008) showed that the predicted concentrations of dark matter only runs are much lower than the ones inferred from X-ray observations of groups and clusters of galaxies.

Additionally, concentration inferred from weak and strong lensing observations can be over estimated due to intrinsic projection effects (Meneghetti et al. 2007) or due to the presence of massive background structures (Coe et al. 2012). When these effects are not correctly taken into account, concentration can have increase of $5 - 6\%$ and the mass estimation can vary up to a factor of 10% (Giocoli et al. 2012).

Most recent high resolution dark matter only simulations showed an upturn trend in the highest mass regime of the mass-concentration relation of simulations at very high redshift (see Zhao et al. 2009; Klypin et al. 2011; Prada et al. 2012). The cause of such upturn is still unclear.

Additionally, the mass-concentration relation of various theoretical and observational studies has a scatter that can span over one order of magnitude. Macciò et al. (2007) proposed that the scatter is partially due the non spherical symmetry of the initial fluctuations, while Neto et al. (2007) (see Fig. 10 in their paper) showed how this scatter can be partially justified by describing the concentration as a function of the formation time of the halo.

Observational studies found that fossil objects (i.e. objects which remain unperturbed for a long period of time) are the objects with the highest value on concentration (Pratt et al. 2016; Kundert et al. 2015; Khosroshahi et al. 2006; Humphrey et al. 2012, 2011; Buote 2017, see). This is in agreement with theoretical studies on unperturbed haloes in dark matter only simulations, where dynamically relaxed haloes have higher concentration than average (Klypin et al. 2016).

Recent works (see e.g. Bhattacharya et al. 2013) fit the concentration as a function of the so called "peak height" ν, where $\nu(M, z) \equiv \delta_{crit}(z)/\sigma(M, z)$, $\delta_{crit} = 1.686$ is the critical density of a collapsing spherical top hat (Gunn & Gott 1972) and $\sigma(M, z)$ is the root mean square density of matter fluctuations over a scale $\propto M^{1/3}$ and redshift z. This relation is very useful for theoretical studies (e.g. dependency between concentration and accretion history). However, comparisons between theory and observations are usually made by comparing mass-concentration relations.

Recent observational studies obtain the density profile of the dark matter component inferring the density profile of the baryon component from X-ray data and remove such component from the total density profiles obtained with gravitational lensing measurements (Du et al. 2015; Merten et al. 2015).

In this work we analyse the concentration of haloes of the Magneticum project suite of simulations (Dolag et al. 2015, 2016). The Magneticum project produced a number of hydrodynamic simulations with different resolutions and ran over different volumes including also dark matter runs. The selection of haloes is discussed in Section 2.

The plan of this paper is as follows. In Section 3 we fit the concentration as a function of mass and redshift and compare our results with other observational and theoretical works. In Section 4 we define the fossilness parameter and show how it increases as the central galaxy of the halo accretes mass and how both the concentration and the fossil parameter change during merging events. We then fit the concentration as a function of the fossilness. In Section 5 we discuss the connection between the concentration and the virial ratio, the energy term from the surface pressure and the fossil parameter. We summarise our conclusions in Section 6.

2 NUMERICAL SIMULATIONS

The Magneticum simulations (www.magneticum.org, Biffi et al. 2013; Saro et al. 2014; Steinborn et al. 2015; Dolag et al. 2016, 2015; Teklu et al. 2015; Steinborn et al. 2016; Bocquet et al. 2016; Remus et al. 2017) is a set of simulations that follow the evolution of overall up to $2 \cdot 10^{11}$ particles of dark matter, gas, stars and black holes on cosmological volumes. The simulations were performed with an extended version of the N−body/SPH code P-Gadget3 which itself is the successor of the code P-Gadget2 (Springel et al. 2005b; Springel 2005). P-Gadget3 uses an improved Smoothed Particle Hydrodynamics (SPH) solver for the hydrodynamics evolution of gas particles presented in Beck et al. (2016). Springel et al. (2005a) describe the treatment of radiative cooling, heating, ultraviolet (UV) back-ground, star formation and stellar feedback processes. Cooling follows 11 chemical elements $(H, He, C, N, O, Ne, Mg, Si, S, Ca, Fe)$ using the publicly available CLOUDY photo-ionisation code (Ferland et al. 1998) while Fabjan et al. (2010); Hirschmann et al. (2014) describe prescriptions for black hole growth and for feedback from AGNs .

Galaxy haloes are identified using a friend-of-friend (FoF) algorithm and sub-haloes are identified using a version of SUBFIND (Springel et al. 2001), adapted by Dolag et al. (2009) to include the baryon component.

The simulations assume a cosmological model in agreement with the WMAP7 results (Komatsu et al. 2011), with total matter density parameter $\Omega_{0,m} = 0.272$, a baryonic fraction of 16.8%, Hubble constant $H_0 = 70.4 \ km/s/Mpc$, index of the primordial power spectrum $n = 0.963$ and a normalisation of the power spectrum corresponding to $\sigma_8 = 0.809$.

In particular, we use three of the Magneticum simulations presented in Table 1. We use Box0/mr to follow the most massive haloes, Box2b/hr to follow haloes within an in-

Table 1. Individual setup of the three Magneticum simulations used in this work. The columns contain the name, the box size, the total number of particles, the mass of each dark matter particle, the initial mass of gas particles, the gravitational softening length of both dark matter and gas ϵ, and the gravitational softening length of star particles $\epsilon_\star$ respectively.

Simulation Name	Size [Mpc/h]	n. part	m_{dm} [$M_\odot/h$]	m_{gas} [$M_\odot/h$]	ϵ [kpc/h]	$\epsilon_\star$ [kpc/h]
Box4/uhr	48	$2 \cdot 576^3$	$3.6 \cdot 10^7$	$7.3 \cdot 10^6$	1.4	0.7
Box2b/hr	640	$2 \cdot 2880^3$	$6.9 \cdot 10^8$	$1.4 \cdot 10^8$	3.75	2
Box/mr	2688	$2 \cdot 4536^3$	$1.3 \cdot 10^{10}$	$2.6 \cdot 10^9$	10	5

Table 2. Number of haloes in each snapshot, that have M_{200} higher than minimum mass for resolved haloes (corresponding to at least 10^4 particles).

		redshift	0	0.5	1	1.5	2
Simulation	Min M_{200} [$M_\odot/h$]	Max M_{200} ($z=0$) [$M_\odot/h$]	n. haloes				
Box4/uhr	$1.3 \cdot 10^{11}$	$1.3 \cdot 10^{14}$	1845	1775	1934	1839	1782
Box2b/hr	$4 \cdot 10^{12}$	$1.8 \cdot 10^{15}$	156110	146339	99669	63542	48925
Box0/mr	$8 \cdot 10^{13}$	$3.8 \cdot 10^{15}$	329648	140560	21274	7792	1112

termediate mass range and Box4/uhr to follow haloes with masses in the galaxy range. From each simulation we selected snapshots nearest to redshifts $z \approx 0, 0.5, 1, 1.5$ and 2. In each snapshot we chose only haloes with a number of dark matter particles greater than 10^4 and then apply a cut in the critical mass so that all objects within this cut are well resolved. Table 2 lists the number of selected haloes, for each simulation and redshift, that match this mass-cut criterion.

3 THE DEPENDENCY OF CONCENTRATION ON MASS AND REDSHIFT

For all selected Magneticum haloes in Table 2, we fit the concentration as a function of mass, using the following functional form:

$$c_{200} = A \cdot \left(\frac{M_{200}}{10^{13} M_\odot} \right)^B . \tag{1}$$

We performed the fit for various redshift bins $z = 0, 0.5, 1, 1.5, 2$ and over the whole range $z = 0 - 2$. The fit was performed using the average concentration computed in 20 logarithmic mass bins that span the whole mass range. The pivot mass $10^{13} M_\odot$ is the median mass of all selected haloes.

When we extract all haloes in a mass range over different snapshots from a simulation, it happens that most haloes at high redshift will be re-selected at lower redshift. We argue that this does not introduce a bias in the selection: in fact, the time between the two snapshots is longer than the dynamical time of the halo, ensuring that there is no correlation between the dynamical states of the two objects after such a long period of time.

Table 3 shows the fit parameters and their errors that are given by the cross-correlation matrix. The concentration at $10^{14} M_\odot$ evolves very weakly with redshift. In order to confirm this, for all selected haloes presented in Table 2, we

also performed a fit of the halo concentration as a power law of mass and redshift using the relation

$$c_{200} = A \cdot \left(\frac{M_{200}}{10^{13} M_\odot} \right)^B \left(\frac{1.47}{1+z} \right)^C . \tag{2}$$

The fit was made on the average concentration of the haloes binned by the 5 redshift bins on the same mass bins as before and for the redshift dependency we use the median redshift value of 1.47 as pivot. The fit, performed over all objects gives:

$$\begin{aligned} A &= 6.02 \pm 0.04 \\ B &= -0.12 \pm 0.01 \\ C &= 0.16 \pm 0.01 \end{aligned} \tag{3}$$

We can see that the redshift dependency, represented by the parameter C, is low although it differs from zero.

Figure 1 shows the mass-concentration plane of Magneticum haloes, where different panels display data at different redshifts. Over-plotted are the fit relations for $c_{200} \propto M_{200}^B$ and $c_{200} \propto M_{200}^B \cdot (1+z)^{-C}$.

Table 4 reports a review of the slope values of the mass-concentration plane found on both theoretical and observational works. Figure 2 shows a plot of the same data. When the slope of the mass-concentration relation had an uncertainty smaller than few percents, we extrapolated the value of the concentration at the mass of $10^{14} M_\odot$ using $h = 0.704$.

Bullock et al. (2001) present one of the first analytical and numerical work on concentration in simulations. They predicted the concentration within the virial radius, that in this work has been converted to a concentration over R_{200}. Although their simulations were performed with a relatively low resolution, their concentration extrapolated at $10^{14} M_\odot$ is within the scatter of present days studies. Neto et al. (2007) employ the first very large dark matter-only N-body cosmological simulation, the Millennium simulation, see Springel (2005) where they constrain the mass-concentration dependency accurately over several orders of magnitudes in mass for dark matter only runs.
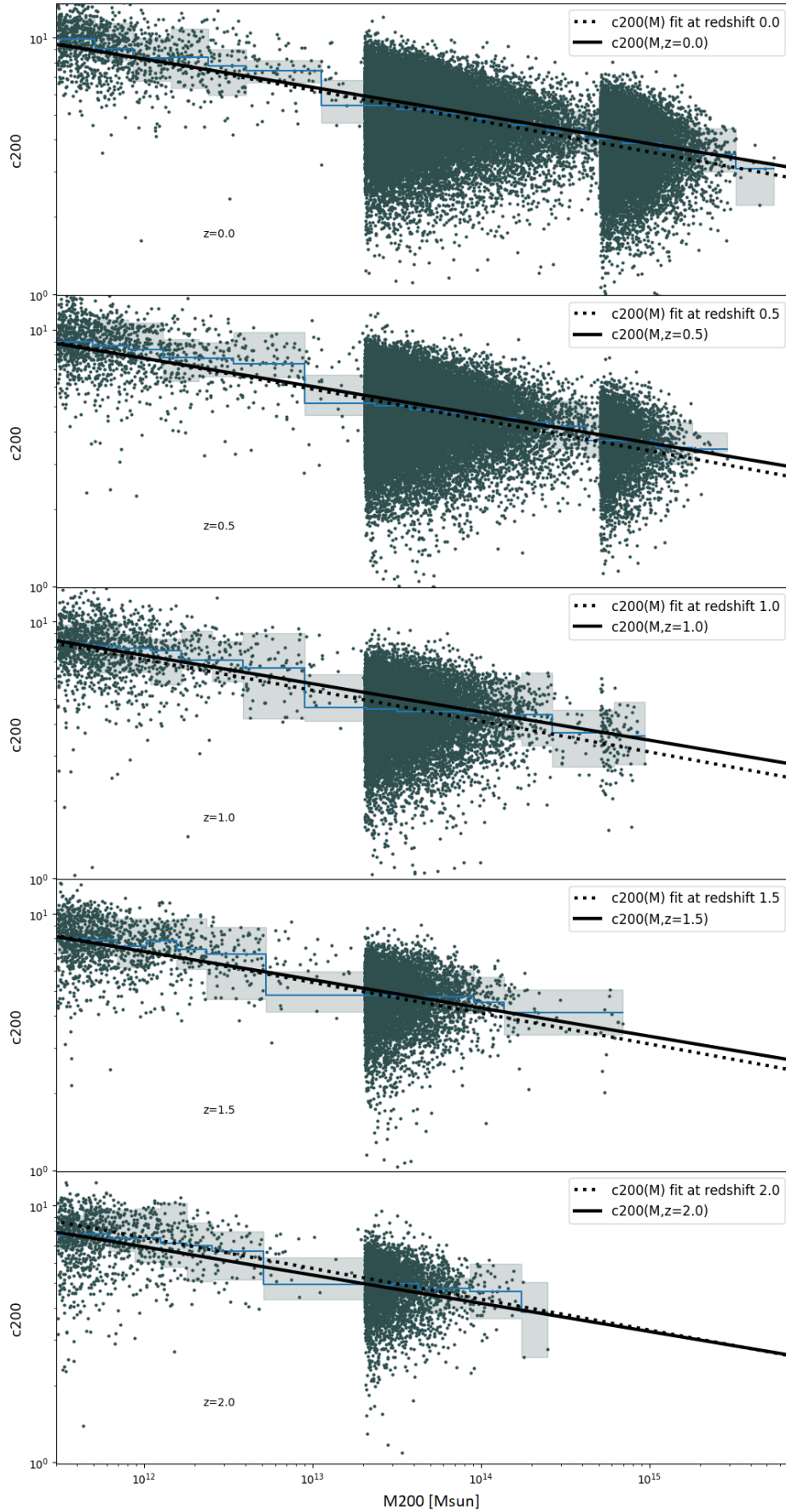
Figure 1. Mass-concentration relation for the well resolved haloes in the three Magneticum simulations Box4/uhr, Box2b/hr and Box0/mr (dark points). Each simulation covers three different mass ranges, respectively $M_{200} > 3 \cdot 10^{11} M_{\odot}$, $M_{200} > 2 \cdot 10^{13} M_{\odot}$ and $M_{200} > 5 \cdot 10^{14} M_{\odot}$. In each panel we show haloes of a different redshift bin, the median of the concentration(blue curve), the locus containing 50% of points (shaded area), the fit obtained with a $c_{200}(M_{200})$ fit as in Equation 1 and $c_{200}(M_{200}, z)$ as in Equation 2 (dotted and solid lines, respectively).

Table 3. Fit parameters of $c_{200}(M_{200})$ as a power law of the halo mass as in Equation 1 for each redshift bin.

redshift	A	B
$z = 0$	6.25 ± 0.07	-0.121 ± 0.004
$z = 0.5$	5.79 ± 0.07	-0.122 ± 0.004
$z = 1$	5.26 ± 0.08	-0.123 ± 0.007
$z = 1.5$	5.36 ± 0.07	-0.117 ± 0.006
$z = 2$	5.37 ± 0.07	-0.097 ± 0.006
$z = 0 - 2$	5.74 ± 0.07	-0.104 ± 0.004

Table 4. Mass ranges and fit parameters of the mass-concentration relation in literature. The value of $c_{200}(10^{14}M_\odot)$ is extrapolated at $z = 0$ when the relative error in the fit parameter is smaller than few percents (when provided). Concentration in Bullock et al. (2001) has been converted from c_{vir} to c_{200}.

authors	mass range $[M_\odot]$			slope	$c_{200}(10^{14}M_\odot)$	comments
Bullock et al. (2001)	10^{11}	$-$	$10^{14}h^{-1}$	≈ -0.3	4.1	N-body
Pratt & Arnaud (2005)	10^{14}	$-$	10^{15}	N/A	$4-6$	X-ray from XMM-Newton
Neto et al. (2007)	10^{12}	$-$	$10^{15}h^{-1}$	-0.1	4.8	N-body from Millennium
Mandelbaum et al. (2008)	10^{12}	$-$	$10^{15}h^{-1}$	-0.13 ± 0.07	4.8	weak lensing via SDSS
Bhattacharya et al. (2013)	$\sim 3 \cdot 10^{12}$	$-$	$10^{15}h^{-1}$	-0.08	4.7	N-body
Martinsson et al. (2013)	10^{11}	$-$	10^{12}	N/A	N/A	Subset of DiskMass survey
Dutton & Macciò (2014)	$10^{12.5}$	$-$	$10^{14.5}h^{-1}$	-0.905	5.2	N-body
Meneghetti et al. (2014)	$6 \cdot 10^{14}$	$-$	$10^{15}h^{-1}$	-0.058	N/A	CLASH mock observations
Ludlow et al. (2014)	10^{12}	$-$	$10^{15}h^{-1}$	-0.1	5.5	N-body from Millennium
Covone et al. (2014)	$3 \cdot 10^{13}$	$-$	$2 \cdot 10^{14}h^{-1}$	0.09	5.4	lensing from CFHTLenS
Correa et al. (2015)		N/A		-0.08	3.8	semi-analytical model
Merten et al. (2015)	$5 \cdot 10^{14}$	$-$	$2 \cdot 10^{15}$	-0.32 ± 0.18	N/A	lensing+X rays on CLASH data
Mantz et al. (2016)	$5 \cdot 10^{14}$	$-$	$2 \cdot 10^{15}$	-0.15	N/A	lensing and X-ray from Chandra and ROSAT on relaxed clusters
Groener et al. (2016)		$\sim 10^{15}$		-0.16	N/A	comprehensive study on lensing data
Klypin et al. (2016)	10^{11}	$-$	$10^{15}h^{-1}$	-0.12	4.1	N-body from MultiDark
Shan et al. (2017)	$5 \cdot 10^{12}$	$-$	$2 \cdot 10^{14}$	-0.13	3.3	weak lensing on SDSS/BOSS
Biviano et al. (2017)	10^{14}	$-$	$2 \cdot 10^{15}$	-0.11 ± 0.1	4.6	dynamics of OmegaWINGS clusters
This work	10^{11}	$-$	10^{15}	-0.1	4.5	Hydro N-body from Magneticum

Pratt & Arnaud (2005) use X-ray data from XMM-Newton, Mandelbaum et al. (2008); Shan et al. (2017) use lensing from SDSS images, while Covone et al. (2014); Mantz et al. (2016); Groener et al. (2016); Covone et al. (2014); Umetsu et al. (2016) combine both lensing and X-ray reconstruction techniques to find the concentration of the dark matter component of haloes. Observations with X-ray data have usually high uncertainties and need to make assumptions on the dependency between the baryon and the dark matter profiles, producing data with large uncertainties. The low mass regime of the plot shows observations of galaxies from the DiskMass survey from Martinsson et al. (2013). Points from the DiskMass survey cover a very large range of concentration values for low massive haloes, in contrast with simulations. Correa et al. (2015) adopted a semi-analytical model (SAM) that predicts concentration over 5 orders of magnitude. Groener et al. (2016) stack all observational mass-concentration data found in literature and made a single fit from it. Klypin et al. (2016) show the results of the MultiDark N-body simulation and produce a lower concentration than Magneticum haloes. Meneghetti et al. (2014) present a numerical work called MUSIC of CLASH where a number of simulated haloes have been chosen to make mock observations for CLASH. Mantz et al. (2016) present results from observations of relaxed haloes. These haloes have a higher concentration in agreement with theoretical studies.

The high mass regime of the plot shows results from observations from WINGS (Biviano et al. 2017) and from CLASH (Merten et al. 2015). It must be taken into account that the galaxies from the DiskMass survey are a restricted subsample of a very large initial sample. Those galaxies have been chosen so that it is possible to compute the concentration. This may have introduced a significant bias in the concentration estimate. Merten et al. (2015); Biviano et al. (2017); Pratt & Arnaud (2005); Martinsson et al. (2013) compute halo properties using dynamical analyses which have larger uncertainties.

Magneticum low-mass haloes have comparatively lower concentration than dark matter only simulations. This is in agreement with other studies that show a lowering of concentration for low-mass haloes when AGN feedback is active (see Duffy et al. 2010).

4   CONCENTRATION AND FOSSIL PARAMETER

The previous section showed how the concentration can span over an order of magnitude on both observational and theoretical works. In this section we show how the scatter is partially related to "how much" a halo is fossil. We first define a fossilness parameter and then study the evolution over time
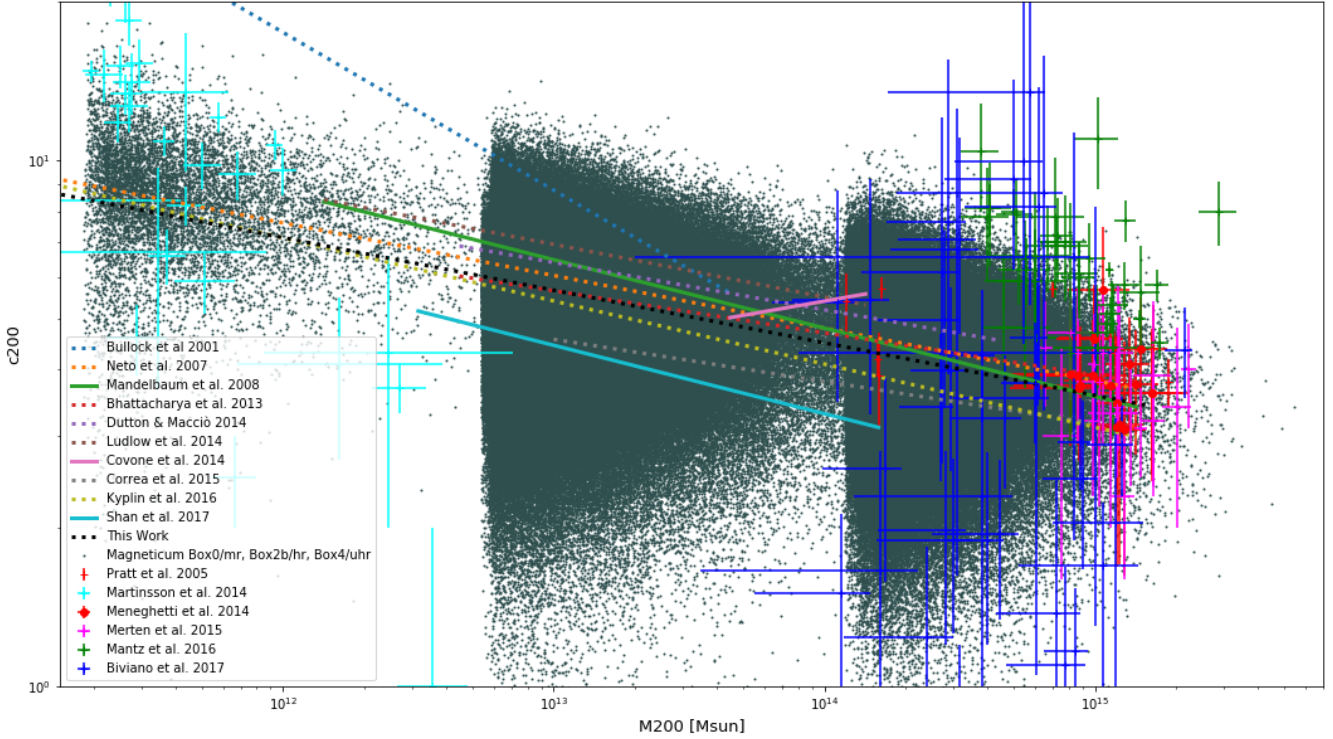
Figure 2. The mass-concentration relation. Grey points are haloes from the Magneticum simulations (see Table 1) at $z = 0$. Black dashed line is the $c_{200}(M_{200})$ median for Magneticum data points. Dashed lines are predictions from simulations and solid lines are fit from observed concentrations, both at $z = 0$. Error bars are from observations from dynamical mass analyses, with no redshift corrections. All mass conversions are made assuming $h = 0.704$.

of both the fossilness and the concentration in some special objects.

Pratt et al. (2016); Kundert et al. (2015); Khosroshahi et al. (2006); Humphrey et al. (2012, 2011); Buote (2017) show how fossil objects have a higher concentration than the average. More generally, simulations found that dynamically relaxed haloes have a higher concentration (see e.g. Klypin et al. 2016).

A fossil object has been defined by Voevodkin et al. (2010) as having a difference in magnitude in the R band $\Delta m_R \geqslant 1.7$ between the most luminous object and the second most luminous object within a distance of $\frac{1}{2}R_{200}$ from the centre.

In our theoretical work we adapt the definition of the fossil parameter by quantifying it as the stellar mass ratio between central galaxy and most massive satellite:

$$\text{fossilness} = \frac{M_{\star,\text{central}}}{\max\{M_{\star,\text{satellite}}\}}. \tag{4}$$

We also extended the search of all satellites to R_{200} (instead of $\frac{1}{2}R_{200}$ proposed by Voevodkin et al. (2010)) because we consider objects outside R_{200} not to contribute to the dynamical state.

We convert the observed magnitude difference to a fossil parameter by assuming a constant ratio between galaxy masses and luminosities,

$$\text{fossilness} = 10^{\Delta m_R/2.5}. \tag{5}$$

This implies that the $\Delta m_R \geqslant 1.7$ threshold defined in Voevodkin et al. (2010) corresponds to a fossilness of

$$\text{fossilness} \gtrsim 4.5. \tag{6}$$

4.1 Concentration evolution in time

In order to understand what brought fossil objects such a high concentration, we followed the evolution of concentration and fossilness for a number of objects in the simulation Box/0mr. We present here two of the few most massive objects at $z = 1.5$ that lived almost un-perturbed until the end of the simulation. They have more than 10^5 particles and a final mass $M_{200} \approx 10^{15} M_\odot$. Figure 3 shows the evolution of halo mass, the stellar mass of central galaxy, scale radius, halo radius, fossilness and concentration of these haloes. In these examples it is very easy to see that as long as their central galaxy accretes satellites and keeps accreting mass, the scale radius decreases and makes their concentration higher and higher.

Additionally, in Figure 4 we show the evolution of two haloes that happen to have only one major merger in their history. When a merger happens then the fossil parameter drops because new massive satellites enter the system and the fossilness value decreases (see Eq. 4). As already expected from previous theoretical studies (Neto et al. 2007) we can see that the concentration goes down.

Neto et al. (2007) showed how the scatter in concentra-
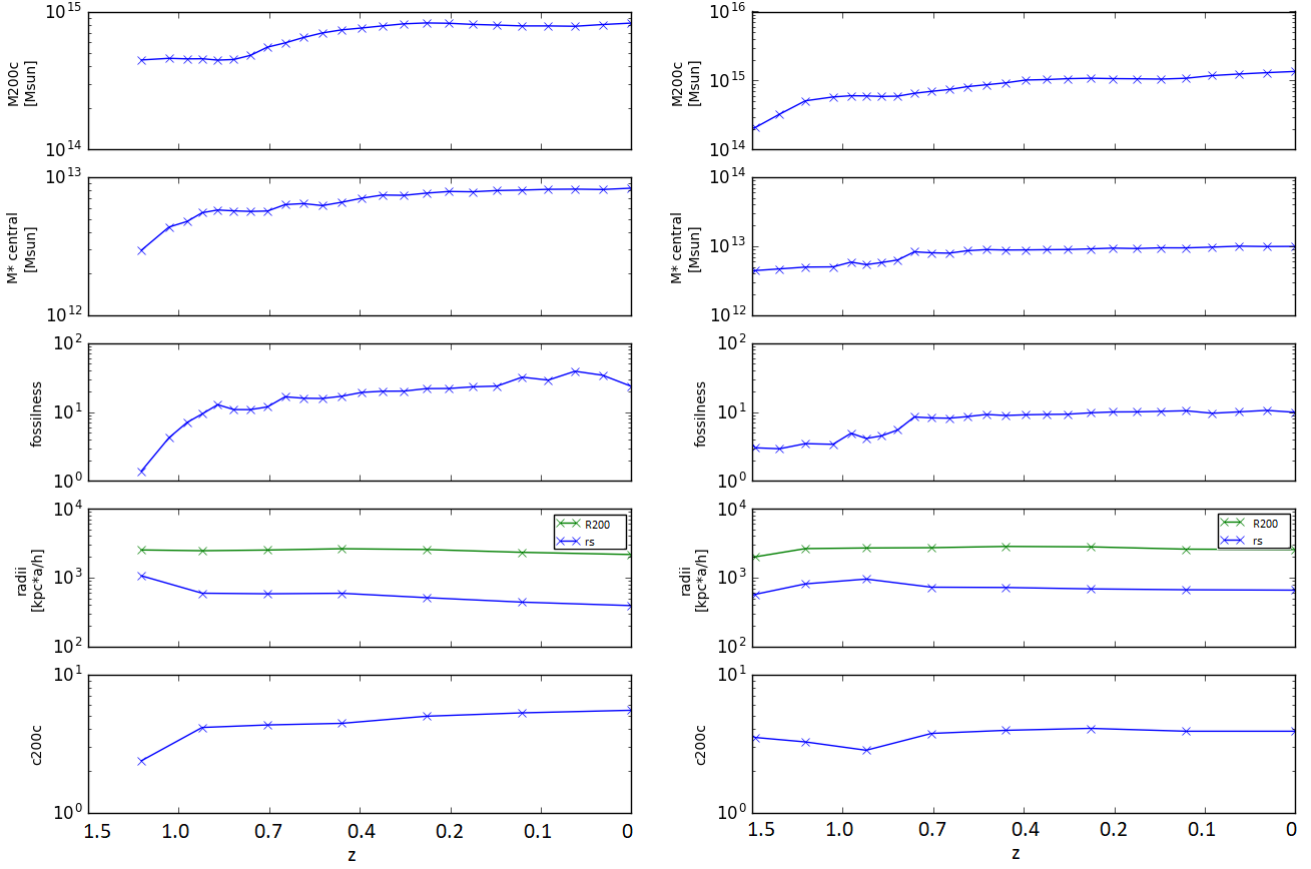
Figure 3. The evolution over time of two haloes (left and right panels) from Box0/mr: M_{200}, stellar mass of central galaxy, fossil parameter, R_{200} (in green) and r_s in (blue) and concentration from to to bottom. Both objects have been selected because they lived unperturbed for most of their time and have no major mergers. As long as their central galaxy accretes satellites and keep accreting mass, the scale radius decreases and in turn, decreases the concentration to decrease, thus the relationship between concentration and fossilness.

tion can be partially described by the formation time, in this subsection we showed how a shift in concentration caused by a slow and steady increase of the concentration (led by a decrease of r_s) brings future fossil groups in the top region of the mass-concentration plane.

## 4.2 Concentration as a function of the fossil parameter

Figure 5 shows the Magneticum haloes concentration as a function of halo mass, colour coded by fossilness. We also show observational data of fossil groups taken from Khosroshahi et al. (2006); Humphrey et al. (2011, 2012); Pratt et al. (2016); Buote (2017) and haloes from Pratt & Arnaud (2005); Biviano et al. (2017); Bartalucci et al. (2018). Since most observational data were provided in terms of R_{500} and c_{500}, in this plot we show mass and concentration computed using $\Delta = 500$ for all data points. Haloes from Biviano et al. (2017) are colour coded by fossilness by converting the difference in magnitude to ratio of luminosities.

Figure 6 shows the concentration distribution for various mass, redshift and colour coded by fossilness bins. We can see that at each mass and redshift bin, the concentration increases with the fossil parameter, while the spread decreases as the fossil parameter increases.

There is a change in slope for very high value of the fossilness parameter so we modelled the dependence of concentration with slopes (see Figure 7, with also the fit results):

$$
\begin{aligned}
c_{200} = &A \cdot \left(\frac{M_{200}}{10^{13} M_\odot} \right)^B \left(\frac{1.47}{1+z} \right)^C \cdot \\
& \cdot \left(\frac{fossilness}{F_0} \right)^D \left(1 + \frac{fossilness}{F_0} \right)^{E-D} .
\end{aligned} \tag{7}
$$

The fit was performed with the binning technique as for the previous fits. Additionally, the fossil parameter was binned over 20 logarithmic bins of $fossilness > 1$. In this case, the exponent E maps the asymptotic exponent of c_{200} for high values of fossil parameters, while D is the exponent for low values of the fossil parameter. The value of F_0 in the fit should should indicate where the two regimes of the fossilness slope starts to change.
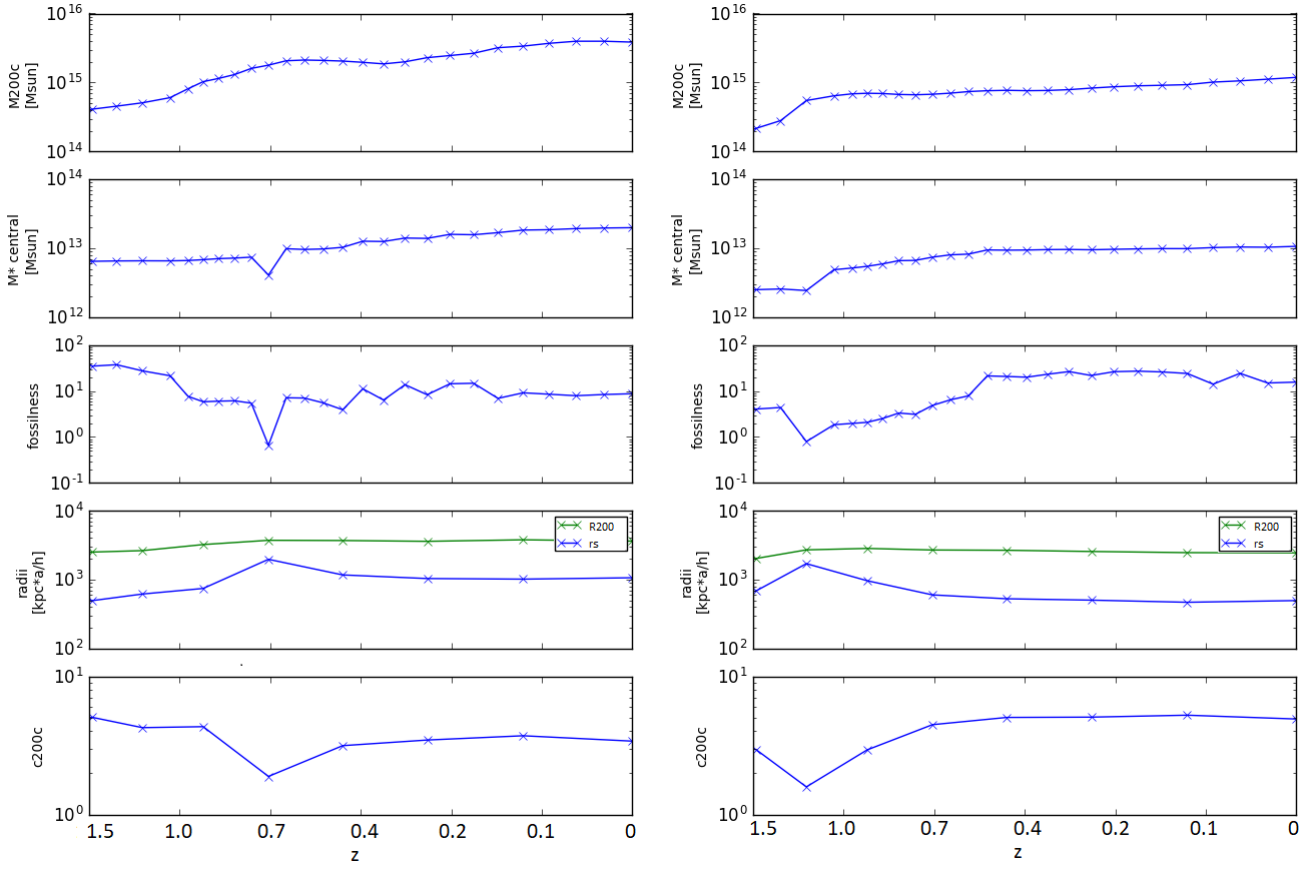
Figure 4. As for Figure 3 but for objects that have a single major merger in their history.

The fit gives the following results:

$$A = 7.5 \pm 0.1$$
$$B = -0.1 \pm 0.1$$
$$C = 0.13 \pm 0.01$$
$$D = 0.40 \pm 0.03 \tag{8}$$
$$F_0 = 4.8 \pm 0.7$$
$$E = -0.015 \pm 0.003$$

Figure 7 shows the fitting relation as well as the data for single haloes and their median. For higher values it is necessary to use a double slope relation.

5   VIRIAL RATIO AND CONCENTRATION

In this section we study how the virial ratio of Magneticum haloes depend on the concentration and fossilness.

The moment of inertia I of a collisionless fluid under a force given by its gravitational potential Φ, obeys the time evolution equation:

$$\frac{1}{2}\frac{d^2I}{dt} = 2K + W - E_s,$$

where the kinetic energy K includes the internal energy of gas, W is the total potential energy of the system and E_s is the energy from the surface pressure P at the halo boundary:

$$E_s = \int_S P(\vec{r})r \cdot d\vec{S}.$$

The pressure takes into account the pressure from the gas component.

A system at the equilibrium is supposed to have the so called virial ratio $\eta = 1$, where

$$\eta \equiv -\frac{2K - E_s}{W}.$$

For more details on how to compute these quantities and integrals see Chandrasekhar (1961); Binney & Tremaine (2008); Cui et al. (2017).

Figure 8 (left panel) shows the ratio $-2K/W$ versus the concentration for the haloes in the Magneticum Box0/mr run while Figure 8 (right panel) shows η versus the concentration. The median η is close to 0.9 and it is generally lower than the median of $-2K/W$. Theoretical works as Klypin et al. (2016) found a lower virial ratio when considering the term E_s. From the figures we can see that there is a correlation between concentration and $-2K/W$, while the correlation is much weaker if we add E_s to the kinetic term.

Figure 9 shows the fossil parameter as a function of E_s/W colour coded by the concentration. Fossil objects have lower E_s (accreting less material from outside) than other clusters, thus their more external region has no activity (no in-fall or outfall of material). This is also in agreement with
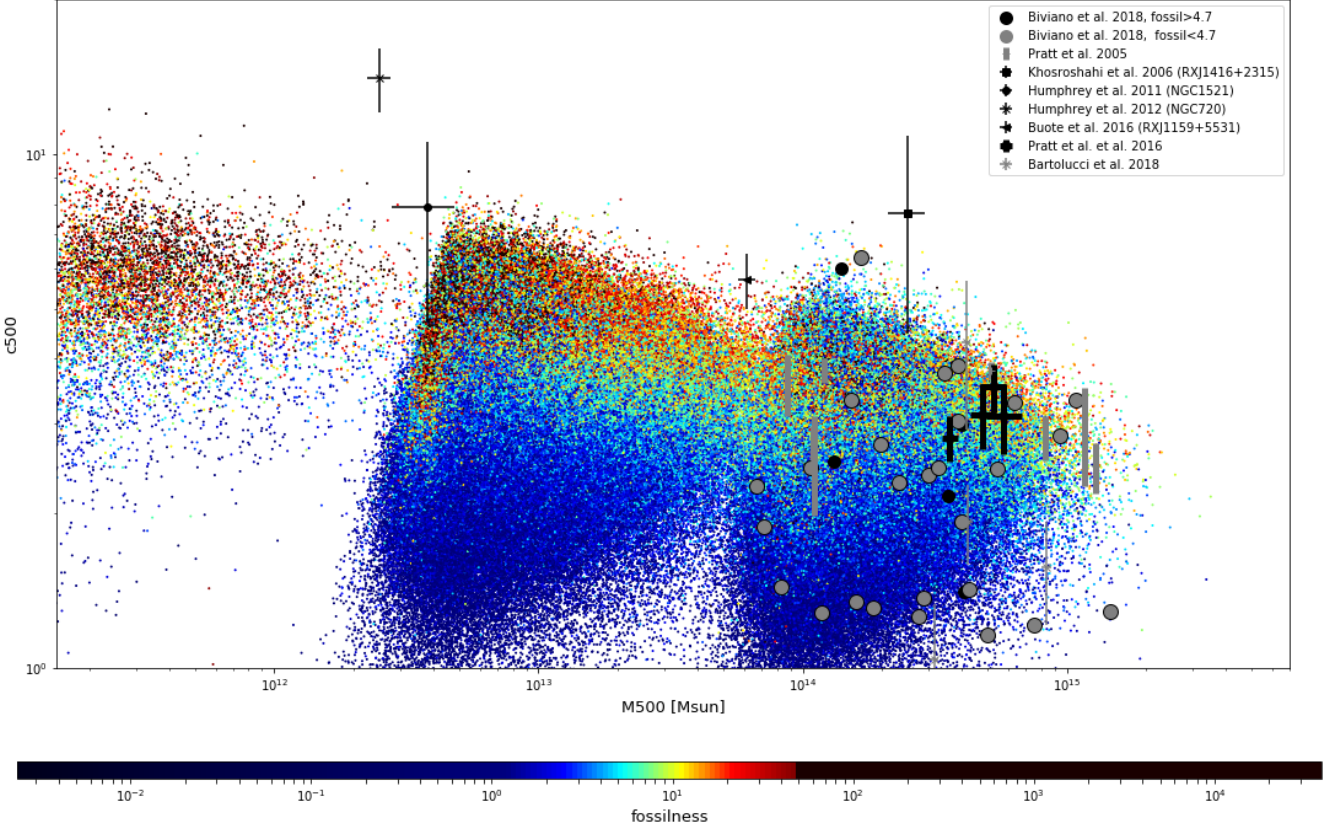
Figure 5. Mass-concentration plane. Mass and radius are computed using Δ_{500}. Points are from the Magneticum data and they are colour coded by fossil parameter (defined as the ratio between stellar masses of the central galaxy and the most massive satellite). The colour saturates to black for the 10% outliers in concentration. Fossil objects from Khosroshahi et al. (2006); Humphrey et al. (2011, 2012); Pratt et al. (2016); Buote (2017) are coloured in black, haloes from Pratt & Arnaud (2005); Bartalucci et al. (2018); Biviano et al. (2017) are coloured in grey. Data from Biviano et al. (2017) is divided between high and low fossilness according to Equation 6.
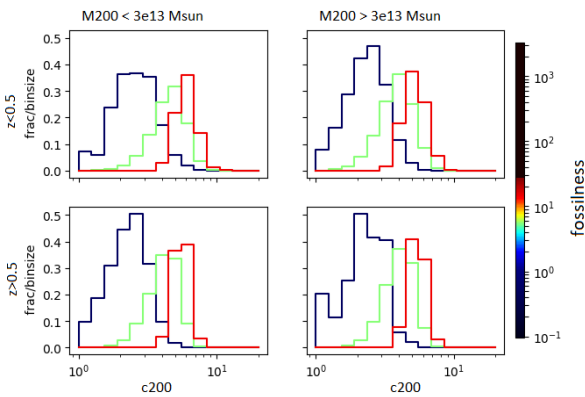
Figure 6. Distribution of concentration for various fossilness values. Left panels contain low mass haloes ($M_{200} < 3 \cdot 10^{13} M_\odot$) and right panels contain high mass haloes ($M_{200} > 3 \cdot 10^{13} M_\odot$), while top row refers to low redshift haloes ($z \leqslant 0.5$) and bottom row refers to high redshift haloes ($z > 0.5$).

Figure 3 where the evolution of fossil concentration is dominated by their internal motions (central galaxy accretes satellites).

6 CONCLUSIONS

We used three cosmological hydrodynamic simulations from the Magneticum suite to cover a mass range from $3 \cdot 10^{11}$ to $6 \cdot 10^{15} M_\odot$ of well resolved clusters from redshift zero to redshift 2 and we computed the concentration for all well resolved haloes and fit it as a power law of mass and redshift.

This is the first study of the mass-concentration relation in hydrodynamic simulations covering several orders of magnitude in mass. For high massive clusters, we found a value of the concentration and its dependency on mass and redshift is in agreement within the large scatter already present in both observations and simulations.

An exception is made for the low mass regime, wherein the Magneticum simulation concentration is systematically lower than concentration found in studies based on dark matter only simulations. Such different behaviour is in agreement with studies of simulations with AGN feedback. They show how the effect of AGN feedback in low mass haloes is capable of lowering the concentration up to a factor of $\approx 15\%$ (see Figure 8 in Duffy et al. 2010) by removing baryons from the inner region of the halo. Thanks to the high mass regime of the Magneticum simulations we are able to capture this effect and its disappearance as the halo mass increases.

In the second part of this work we discussed the origin of
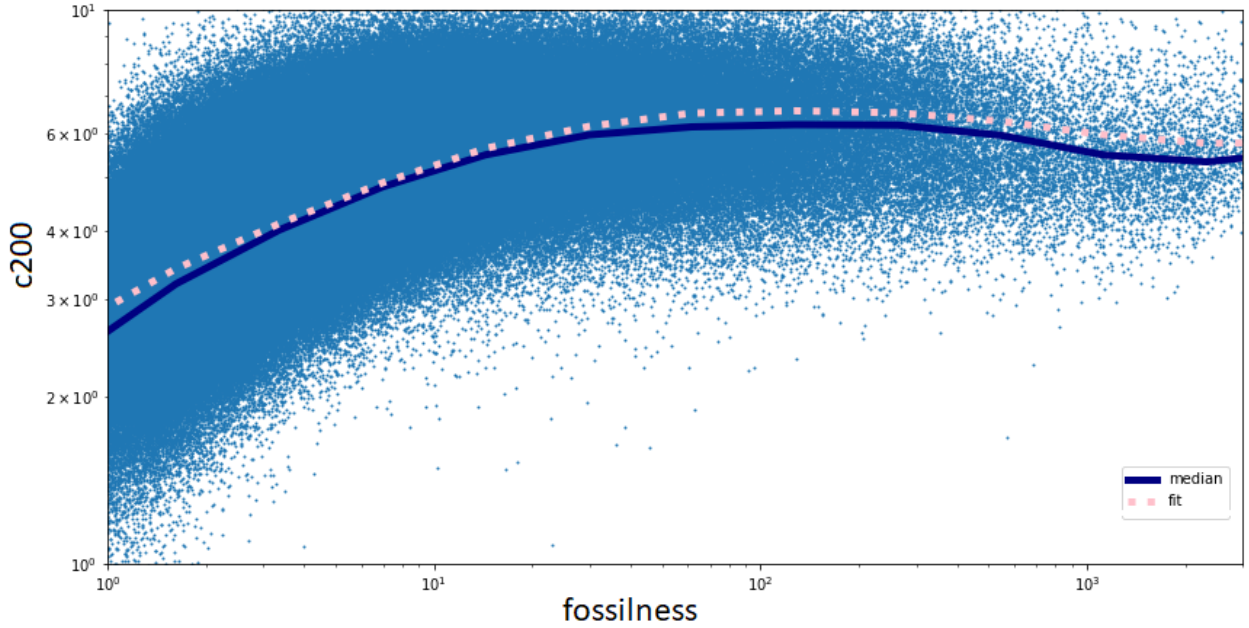
Figure 7. Concentration vs. fossilness for Magneticum data. Over plotted are the median, the concentration depending a double power law of the fossilness.
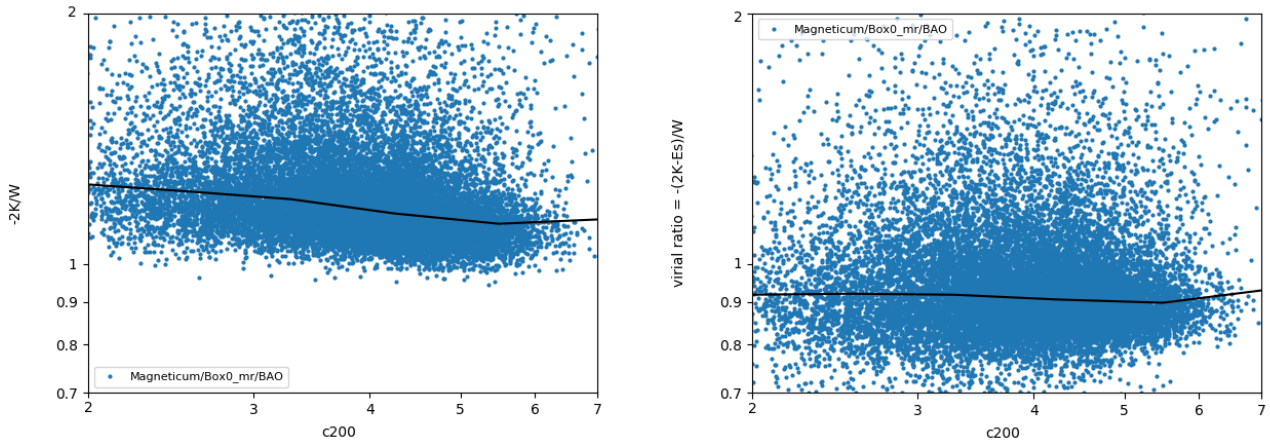
Figure 8. Virial ratio without (left panel) and with (right panel) the correction from the pressure term, as a function of the concentration for the simulation Magneticum/Box0/mr.

the large scatter of concentration in the mass-concentration plane by studying its dependency on the fossilness. Fossil groups are supposed to have had a long period of inactivity and are known to have a higher concentration (see e.g. Neto et al. 2007; Dutton & Macciò 2014; Pratt et al. 2016). Since we are working with hydrodynamic simulations, we were able to compute the halo fossilness exploiting the stellar masses of galaxies (see Eq. 4) and to compare our values to observations.

We showed that when a halo is left unperturbed, both fossilness and concentration steadily and slowly grow with time. This is in contrast with more naive models where an unperturbed halo keeps its concentration making it a mere function of its collapse time (as in Bullock et al. 2001). In-

terestingly, we found that this change of concentration is due to a decline of the scale radius. We also showed how the scale radius and fossilness increase or decrease together when a major merger occurs (see Figure 4). From these analyses, we found that those two effects drive the correlation between concentration and fossil parameter.

Our findings are not in contrast with the fact that relaxed and fossil objects start with a high concentration because of their early formation times, but we show how an additional steady increase of the concentration pushes these objects in the very high region of the mass-concentration plane.

The correlation between concentration and fossilness
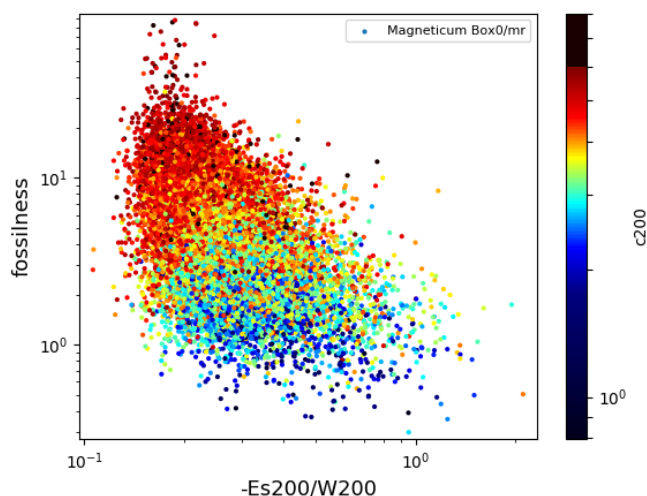
Figure 9. Fossilness versus virial ratio for Magneticum/Box0/bao run, colour coded by concentration (colour bar on the right). The colour saturates to black for the 10% outliers in concentration.

saturates after $fossilness \approx 20 - 30$ (see the plateau in Figure 7) and we provide a double power law fit parameters.

We then examined the concentration as a function of the virial ratio $\eta = -(2K - E_s)/W$ and as a function of the energy from the surface pressure. We found a weak dependency of the concentration on $-(2K - E_s)/W$ and very weak on the terms $-2K/W$ and E_s. The difference between $-2K/W$ and $-(2K - E_s)/W$ is higher for haloes with lower concentration. This implies that low concentration objects are accreting material from the outside and it is in agreement with the idea that low-concentration haloes are not relaxed. This is compatible with other theoretical works as Klypin et al. (2016).

In Figure 9 we showed how the fossil parameter, the concentration and E_s are interconnected. A large value of E_s means that the cluster has a considerable amount of infalling material and this translates into a low concentration and low fossil parameter; while a low value of E_s (no infalling material) can be related to both high and low concentrated clusters. Fossil objects have a lower value of E_s indicating a a low accretion rate.

Work has still to be done to study the relation between fossil parameter and other quantities that are well known to be tied with the dynamical state of a system, for instance, the difference between centre of mass and density peak position), or the velocity dispersion deviation between the one inferred from the virial theorem. Additional work is also needed in order to understand the connection between central galaxy accreting satellites and the redistribution of the angular momentum within the halo, which in turn may give hints on the weak dependency between concentration and spin parameter (as found by Macciò et al. 2008).

REFERENCES

Bartalucci I., Arnaud M., Pratt G. W., Le Brun A. M. C., 2018, A&A, 617, A64
Beck A. M., et al., 2016, MNRAS, 455, 2110
Bhattacharya S., Habib S., Heitmann K., Vikhlinin A., 2013, ApJ, 766, 32
Biffi V., Dolag K., Böhringer H., 2013, MNRAS, 428, 1395
Binney J., Tremaine S., 2008, Galactic Dynamics: Second Edition. Princeton University Press
Biviano A., et al., 2017, A&A, 607, A81
Bocquet S., Saro A., Dolag K., Mohr J. J., 2016, MNRAS, 456, 2361
Borgani S., Kravtsov A., 2011, Advanced Science Letters, 4, 204
Bullock J. S., Kolatt T. S., Sigad Y., Somerville R. S., Kravtsov A. V., Klypin A. A., Primack J. R., Dekel A., 2001, MNRAS, 321, 559
Buote D. A., 2017, ApJ, 834, 164
Chandrasekhar S., 1961, Hydrodynamic and hydromagnetic stability
Coe D., et al., 2012, ApJ, 757, 22
Correa C. A., Wyithe J. S. B., Schaye J., Duffy A. R., 2015, MNRAS, 452, 1217
Covone G., Sereno M., Kilbinger M., Cardone V. F., 2014, ApJ, 784, L25
Cui W., Power C., Borgani S., Knebe A., Lewis G. F., Murante G., Poole G. B., 2017, MNRAS, 464, 2502
De Boni C., 2013, preprint, (arXiv:1302.2364)
De Boni C., Ettori S., Dolag K., Moscardini L., 2013, MNRAS, 428, 2921
Dolag K., Bartelmann M., Perrotta F., Baccigalupi C., Moscardini L., Meneghetti M., Tormen G., 2004, A&A, 416, 853
Dolag K., Borgani S., Murante G., Springel V., 2009, MNRAS, 399, 497
Dolag K., Gaensler B. M., Beck A. M., Beck M. C., 2015, MNRAS, 451, 4277
Dolag K., Komatsu E., Sunyaev R., 2016, MNRAS, 463, 1797
Du W., Fan Z., Shan H., Zhao G.-B., Covone G., Fu L., Kneib J.-P., 2015, ApJ, 814, 120
Duffy A. R., Schaye J., Kay S. T., Dalla Vecchia C., 2008, MNRAS, 390, L64
Duffy A. R., Schaye J., Kay S. T., Dalla Vecchia C., Battye R. A., Booth C. M., 2010, MNRAS, 405, 2161
Dutton A. A., Macciò A. V., 2014, MNRAS, 441, 3359
Fabjan D., Borgani S., Tornatore L., Saro A., Murante G., Dolag K., 2010, MNRAS, 401, 1670
Ferland G. J., Korista K. T., Verner D. A., Ferguson J. W., Kingdon J. B., Verner E. M., 1998, PASP, 110, 761
Giocoli C., Meneghetti M., Ettori S., Moscardini L., 2012, MNRAS, 426, 1558
Groener A. M., Goldberg D. M., Sereno M., 2016, MNRAS, 455, 892
Gunn J. E., Gott III J. R., 1972, ApJ, 176, 1

Hirschmann M., Dolag K., Saro A., Bachmann L., Borgani S., Burkert A., 2014, MNRAS, 442, 2304

Humphrey P. J., Buote D. A., Canizares C. R., Fabian A. C., Miller J. M., 2011, ApJ, 729, 53

Humphrey P. J., Buote D. A., O'Sullivan E., Ponman T. J., 2012, ApJ, 755, 166

Khosroshahi H. G., Maughan B. J., Ponman T. J., Jones L. R., 2006, MNRAS, 369, 1211

Klypin A. A., Trujillo-Gomez S., Primack J., 2011, ApJ, 740, 102

Klypin A., Yepes G., Gottlöber S., Prada F., Heß S., 2016, MNRAS, 457, 4340

Komatsu E., et al., 2011, ApJS, 192, 18

Kundert A., et al., 2015, MNRAS, 454, 161

Lin W. P., Jing Y. P., Mao S., Gao L., McCarthy I. G., 2006, ApJ, 651, 636

Ludlow A. D., Navarro J. F., Li M., Angulo R. E., Boylan-Kolchin M., Bett P. E., 2012, MNRAS, 427, 1322

Ludlow A. D., Navarro J. F., Angulo R. E., Boylan-Kolchin M., Springel V., Frenk C., White S. D. M., 2014, MNRAS, 441, 378

Macciò A. V., Dutton A. A., van den Bosch F. C., Moore B., Potter D., Stadel J., 2007, MNRAS, 378, 55

Macciò A. V., Dutton A. A., van den Bosch F. C., 2008, MNRAS, 391, 1940

Mandelbaum R., Seljak U., Hirata C. M., 2008, J. Cosmology Astropart. Phys., 8, 006

Mantz A. B., Allen S. W., Morris R. G., 2016, MNRAS, 462, 681

Martinsson T. P. K., Verheijen M. A. W., Westfall K. B., Bershady M. A., Andersen D. R., Swaters R. A., 2013, A&A, 557, A131

Meneghetti M., Rasia E., 2013, preprint, (arXiv:1303.6158)

Meneghetti M., Argazzi R., Pace F., Moscardini L., Dolag K., Bartelmann M., Li G., Oguri M., 2007, A&A, 461, 25

Meneghetti M., et al., 2014, ApJ, 797, 34

Merten J., et al., 2015, ApJ, 806, 4

Naderi T., Malekjani M., Pace F., 2015, MNRAS, 447, 1873

Navarro J. F., Frenk C. S., White S. D. M., 1996, ApJ, 462, 563

Navarro J. F., Frenk C. S., White S. D. M., 1997, ApJ, 490, 493

Neto A. F., et al., 2007, MNRAS, 381, 1450

Prada F., Klypin A. A., Cuesta A. J., Betancort-Rijo J. E., Primack J., 2012, MNRAS, 423, 3018

Pratt G. W., Arnaud M., 2005, A&A, 429, 791

Pratt G. W., Pointecouteau E., Arnaud M., van der Burg R. F. J., 2016, A&A, 590, L1

Remus R.-S., Dolag K., Naab T., Burkert A., Hirschmann M., Hoffmann T. L., Johansson P. H., 2017, MNRAS, 464, 3742

Saro A., et al., 2014, MNRAS, 440, 2610

Shan H., et al., 2017, ApJ, 840, 104

Springel V., 2005, MNRAS, 364, 1105

Springel V., White S. D. M., Tormen G., Kauffmann G., 2001, MNRAS, 328, 726

Springel V., Di Matteo T., Hernquist L., 2005a, MNRAS, 361, 776

Springel V., et al., 2005b, Nature, 435, 629

Steinborn L. K., Dolag K., Hirschmann M., Prieto M. A., Remus R.-S., 2015, MNRAS, 448, 1504

Steinborn L. K., Dolag K., Comerford J. M., Hirschmann M., Remus R.-S., Teklu A. F., 2016, MNRAS, 458, 1013

Teklu A. F., Remus R.-S., Dolag K., Beck A. M., Burkert A., Schmidt A. S., Schulze F., Steinborn L. K., 2015, ApJ, 812, 29

Umetsu K., Zitrin A., Gruen D., Merten J., Donahue M., Postman M., 2016, ApJ, 821, 116

Voevodkin A., Borozdin K., Heitmann K., Habib S., Vikhlinin A., Mescheryakov A., Hornstrup A., Burenin R., 2010, ApJ, 708, 1376

Zhao D. H., Jing Y. P., Mo H. J., Börner G., 2009, ApJ, 707, 354